npj | spintronics

www.nature.com/npjspintronics

ARTICLE OPEN

Check for updates

A first-principles study of bilayer 1*T*′-WTe_2/CrI_3: a candidate topological spin filter

Daniel Staros[1]✉, Brenda Rubenstein[1]✉ and Panchapakesan Ganesh[2]✉

The ability to manipulate electronic spin channels in 2D materials is crucial for realizing next-generation spintronics. Spin filters are spintronic components that polarize spins using external electromagnetic fields or intrinsic material properties like magnetism. Recently, topological protection from backscattering has emerged as an enticing feature that can be leveraged to enhance the robustness of 2D spin filters. In this work, we propose and then characterize one of the first 2D topological spin filters: bilayer CrI_3/1*T*′-WTe_2. To do so, we use a combination of density functional theory, maximally localized Wannier functions, and quantum transport calculations to demonstrate that a terraced bilayer satisfies the principal criteria for being a topological spin filter: namely, that it is gapless, exhibits spin-polarized charge transfer from WTe_2 to CrI_3 that renders the bilayer metallic, and has a topological boundary which retains the edge conductance of monolayer 1*T*′-WTe_2. In particular, we observe that small negative ferromagnetic moments are induced on the W atoms in the bilayer, and the atomic magnetic moments on the Cr are approximately 3.2 μ_B/Cr compared to 2.9 μ_B/Cr in freestanding monolayer CrI_3. Subtracting the charge and spin densities of the constituent monolayers from those of the bilayer further reveals spin-orbit coupling-enhanced spin-polarized charge transfer from WTe_2 to CrI_3. We demonstrate that the bilayer is topologically trivial by showing that its Chern number is zero. Lastly, we show that interfacial scattering at the boundary between the terraced materials does not remove WTe_2's edge conductance. Altogether, this evidence indicates that BL 1*T*′-WTe_2/CrI_3 is gapless, magnetic, and topologically trivial, meaning that a terraced WTe_2/CrI_3 bilayer heterostructure in which only a portion of a WTe_2 monolayer is topped with CrI_3 is a promising candidate for a 2D topological spin filter. Our results further suggest that 1D chiral edge states may be realized by stacking strongly ferromagnetic monolayers, like CrI_3, atop 2D nonmagnetic Weyl semimetals like 1*T*′-WTe_2.

npj Spintronics (2024)2:4 ; https://doi.org/10.1038/s44306-023-00007-y

INTRODUCTION

As signs continue to suggest that Moore's Law has plateaued, researchers have begun to seek new routes to designing faster, smaller, more energy-efficient, and more versatile electronic devices. The key to realizing such devices will be discovering, characterizing, and designing novel nanoscale quantum electronic components whose many electronic degrees of freedom, including their electron spin[1,2] and momenta[3,4], can be manipulated to enable faster, more energy-efficient operations on denser data.

Along these lines, nanoscale spintronics have been hailed as extremely promising routes towards denser data storage and potentially faster and more efficient reading and writing. Unlike conventional electronics, which harness the charge of an electron, spintronic materials store information in electrons' two possible spin states[1], which can be manipulated more rapidly and with less energy than electrons' charges[5]. Spintronic devices are also less volatile than conventional electronic devices because they can preserve their spin even in the absence of electric power[1,6]. Moreover, one of the primary advantages of spintronic devices is that they can be readily integrated into modern CMOS-based circuits[6].

Since the birth of spintronics with the discovery of the giant magnetoresistive effect[1], the world of spintronic device components has expanded to include various spintronic analogs to traditional resistors and transistors, as well as new components unique to controlling spin currents like spin filters and spin injectors[7]. Many of these components take advantage of the properties of magnetic materials, in which spins are already selectively ordered. For example, two spintronic analogs to traditional resistors, spin valves and magnetic tunnel junctions (MTJs), typically consist of two ferromagnetic layers separated by an insulating layer[6,7]. Varying the magnetic orientation of one of the magnetic layers and keeping the other fixed allows the resistance to spin currents to be changed by taking advantage of spin-selective quantum tunneling as in MTJs, or the giant magnetoresistive or spin-transfer torque effects as in spin valves. Perhaps the most fundamental spintronic device component, however, is that which enables the generation of spin current in the first place: the spin filter.

Spin filters are devices that generate spin-polarized currents from unpolarized electric currents by selectively transmitting electrons with a particular spin and blocking those with the opposite spin. In general, such devices have most often taken advantage of the inherent spin polarization in ferromagnetic or multiferroic materials[8–10], spin-selective quantum tunneling using barrier materials with different spin-dependent transmission probabilities[11], or spin-orbit coupling in Rashba-type spin filters to achieve this[12,13]. Spin filters can additionally be designed by placing ferromagnetic insulators in close proximity to superconducting junctions since the presence of an out-of-plane magnetic field can break time-reversal symmetry, causing the electrons to form spin-polarized currents through the spin-transfer torque effect[14–16].

[1]Department of Chemistry, Brown University, Providence, RI 02912, USA. [2]Center for Nanophase Materials Sciences, Oak Ridge National Laboratory, Oak Ridge, TN 37831, USA. ✉email: daniel_staros@brown.edu; brenda_rubenstein@brown.edu; ganeshp@ornl.gov

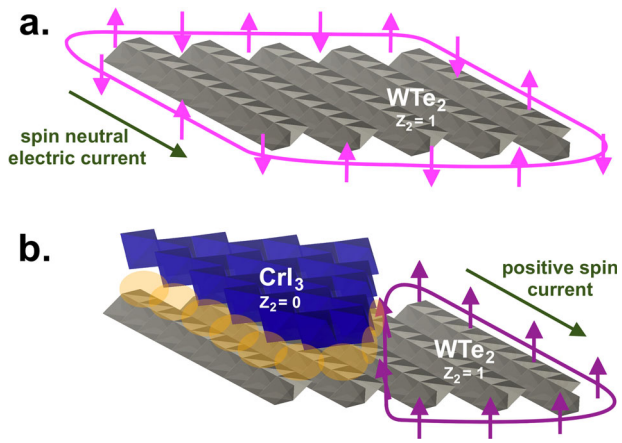

Fig. 1 Schematics of the edge conductance in the materials studied in this manuscript. a Edge conductance around ML WTe_2. **b** Proposed spin-polarized edge conductance/1D chiral edge state of the CrI_3/WTe_2 bilayer studied here.

Recently, the concept of topological spin filters has been put forth as one promising option for improving the robustness of spin filters at higher temperatures by taking advantage of quantum anomalous Hall conductance, which is topologically protected from backscattering and could minimize dissipation as a result. By extension, edge conductance dominated by one spin channel amounts to nearly dissipationless conductance of one direction of quantum spin, also known as topological spin filtering, which can manifest as a chiral edge state along the edge of a partially exposed topologically trivial bilayer and nontrivial monolayer (see Fig. 1)[17]. The magnetic Weyl semimetal $Co_3Sn_2S_2$ has recently been discussed as a potential avenue towards realizing such higher temperature chiral conducting edge states[17,18], which could in principle also become spin-polarized. Along the same vein, a topological spin filter may be constructed by placing a ferromagnet near topologically nontrivial 2D materials such as 1T' transition metal dichalcogenides[19], which could also give rise not only to spin-polarized currents, but spin-polarized helical edge modes that are topologically protected from backscattering.

While many such three-dimensional spin filters have been proposed, two-dimensional materials and their heterostructures possess a larger design space advantageous for engineering new spintronic devices[20]. Two-dimensional heterostructures can be designed to exhibit a wide array of emergent properties by mixing and matching the properties of their constituent monolayers[21,22], twisting them[23–26], straining them[27], or placing them in proximity to electric and/or magnetic fields[28–31]. Despite this, researchers have only recently made significant strides towards truly 2D spin filters which promise to be smaller, more tunable, and ideally more efficient than their 3D counterparts. Graphene is one 2D material that originally garnered spintronic interest when it was predicted to exhibit nearly perfect spin filtering when interfaced with only a couple of layers of a ferromagnetic metal[32]. However, experimental attempts to realize such a graphene-based spin filter fell short, initially showing tunnel magnetoresistance ratios of 0.4% for graphene/NiFe, with additional attempts increasing this ratio to no more than 5%[2,33,34]. More recently, the pivotal discovery of giant magnetoresistance in bilayer CrI_3 in 2018 has reinvigorated the search for better 2D spin filters based on atomically thin magnets[35–38], and a slew of inspired studies have since been published that take advantage of their properties[38–42]. These examples suggest that, with the right combination of 2D monolayers, 2D spin filters, and even 2D topological spin filters, should also be within reach.

Notably, there are few studies that consider the proximity effects of 2D magnets stacked atop a monolayer of 1T'-WTe_2, which is the only MX_2 monolayer that exists in the 1T' phase in its ground state and the only such member that is topological as a freestanding monolayer[43]. Until fairly recently, the only such example consisted of one layer of 1T'-WTe_2 interfaced with one layer of permalloy ($Ni_{80}Fe_{20}$) to form a film with a several-nm thickness that exhibited out-of-plane magnetic anistropy[44,45]. More recently, proximity-induced magnetic order was observed in monolayer 1T'-WTe_2 placed onto antiferromagnetic trilayer CrI_3, where edge conductance jumps were observed upon switching of CrI_3's magnetic state[46,47]. Most recently, proximity-induced half-metallicity and complete spin polarization were predicted in bilayer 1T'-$WTe_2/CrBr_3$ and attributed to strong orbital hybridization and charge transfer at the interface of the heterostructure[48]. Nonetheless, to the best of our knowledge, no investigation of the topological properties of a 1T'-WTe_2/CrX_3 bilayer has yet been performed, let alone with the goal of realizing a new type of *topological* spin filter. Taken together, these discoveries point towards bilayer 1T'-WTe_2/CrI_3 as a strong potential candidate for topological spin filtering, which could leverage the perfect spin filtering of a 1T'-WTe_2/CrX_3 hetrostructure in proximity to the dissipationless edge states of 1T'-WTe_2.

Thus, in this manuscript, we use ab initio and quantum transport simulations to identify terraced bilayer 1T'-WTe_2/CrI_3 as a promising candidate for a 2D topological spin filter. 1T'-WTe_2 is a nonmagnetic Weyl semimetal that exhibits topological edge conductance in its monolayer form[19], while monolayer CrI_3 is a ferromagnetic Mott insulator[49]. One can thus imagine that, by placing these two materials in proximity, the CrI_3's magnetism could potentially polarize WTe_2's edge conductance, forming a topological spin filter. To determine whether this is in fact the case, we predict the charge and magnetization density transfer, band structures, and topological invariants for BL CrI_3/1T'-WTe_2 with and without spin-orbit coupling. In so doing, we unequivocally demonstrate that the proximity of CrI_3 to WTe_2 foremost results in strong interlayer coupling between the two layers, spin polarization on the WTe_2, and an overall trivial BL topology. To determine whether edge conductance is lost in a terraced bilayer, we also predict the conduction in a model terraced bilayer, showing that spin-polarized edge conductance is retained. These considerations, taken together with the metallic nature of the bilayer and previous evidence for spin-polarized helical edge modes in monolayer 1T'-WTe_2, provide convincing evidence for the possibility of realizing chiral edge states at the interface of a terraced 1T'-WTe_2/CrI_3 bilayer. Specifically, our results imply that electric current injected into the metallic bilayer portion of the terraced heterostructure would become spin-polarized before transferring to WTe_2 and exiting via spin-polarized edge conductance in chiral edge states around the monolayer WTe_2 portion; this terraced, strained 1T'-WTe_2/CrI_3 bilayer is then likely a strong candidate for a highly robust, ultra-thin spin filter with 1D chiral edge states.

RESULTS

Interlayer charge transfer and magnetic induction

As a first step toward understanding the physics of our bilayer, we began by examining how the layers influence each other's electronic structure. To do so, we analyzed the difference between the bilayer and individual monolayers' charge and spin densities. If proximity effects are truly at play, we would expect to see significant differences in their bilayer charge and spin densities relative to the separate monolayer densities. That said, when a monolayer of CrI_3 is stacked on a monolayer of 1T'-WTe_2, the density functional theory (DFT)-predicted charge density difference between the bilayer and monolayers, $\rho_{BL} - \rho_{CrI3} - \rho_{WTe2}$,

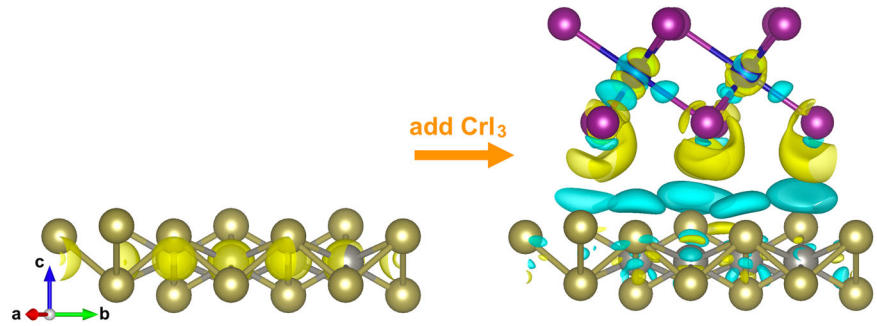

Fig. 2 Charge transfer upon placing monolayer CrI_3 onto monolayer WTe_2. Left: Collinear PBE charge density of monolayer WTe_2 in the absence of CrI_3 with an isosurface level value of 0.8. **Right:** Collinear PBE+U charge density difference between the bilayer and individual monolayers, $\rho_{BL} - \rho_{CrI3} - \rho_{WTe2}$, with an isosurface level value of 0.0025. Charge transfer from WTe_2 to CrI_3 is evident. Yellow indicates a positive charge density and light blue indicates a negative charge density. Chromium atoms are colored dark blue and iodine atoms are purple, while tungsten atoms are gray and tellurine atoms are beige.

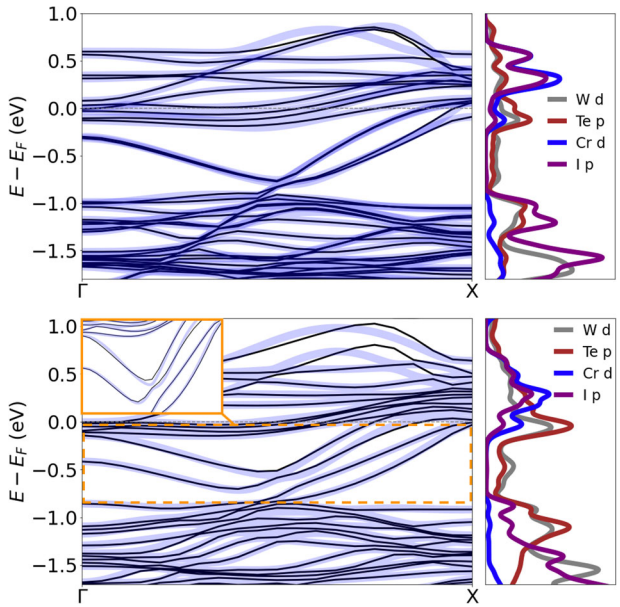

Fig. 3 Band structures of bilayer 1T′-WTe_2/CrI_3. Top: Collinear PBE+U band structure (black) and partial density of states (PDOS) of bilayer 1T'-WTe_2/CrI_3 with the interpolated MLWF band structures overlain (light blue). **Bottom:** Noncollinear PBE+U band structure with spin-orbit coupling.

clearly shows charge accumulating near the CrI_3/WTe_2 interface as the charge is drawn downwards (see Fig. 2). This suggests that CrI_3 is a charge acceptor and WTe_2 is a charge donor in the bilayer. We see this charge transfer effect both with (noncollinear calculations) and without (collinear calculations) including spin-orbit coupling (SOC) in our DFT calculations (see Supplementary Fig. 3), suggesting that it is a robust feature of the bilayer.

Interestingly, charge also accumulates in between and around the bilayer with charge accumulating near the CrI_3 within the vdW interface, and withdrawn from the portion of CrI_3, which is facing away from the interface. The existence of significant charge density within the bilayer gap confirms the strong hybridization between the iodine and tellurium atoms, which is also reflected in the significant atomic overlaps of all four atomic species in the partial densities of states or PDOS (see Fig. 3). In addition, the metallicity of the bilayer is reflected in the PDOS occupations of all four atomic species at and near the Fermi level, indicating that this hybridization causes CrI_3 to lose its Mott insulating nature when it is interfaced with WTe_2. The Lowdin charges of the constituent monolayers and bilayer are tabulated in Supplementary Tables I and III to quantify the extent of charge transfer in this bilayer. Summing the individual atomic charges of the monolayers and the bilayer yields an electron transfer of approximately 0.06 e per primitive bilayer cell.

Lastly, we consider the spin polarization that accompanies these charge transfer effects by evaluating the collinear spin density difference $s_{BL} - s_{CrI3} - s_{WTe2}$ and the z-component of the noncollinear magnetization density difference $m_{BL} - m_{CrI3} - m_{WTe2}$ between the bilayer and individual monolayers. We find that charge transfer in the absence of SOC is minimally spin polarized, though the collinear spin density difference indicates that the Cr moments become slightly larger, which can be attributed to charge transfer with a slightly larger spin-up character (see Fig. 4). Strikingly, the charge transfer we observe is significantly more spin-polarized when SOC is considered. The charge transfer is mostly spin-up as in the collinear case, but to such a large extent that the W atoms in WTe_2 become polarized in the opposite, spin-down direction. We attribute this to the SOC-enhanced splitting of WTe_2's majority up and down spin bands, which yields majority down spin WTe_2 bands that are lower in energy than its up spin bands similar to that observed in bilayer 1T'-WTe_2/$CrBr_3$[48]. This change is additionally accompanied by an increase in the magnitude of the bilayer Cr magnetic moments relative to those in monolayer CrI_3 with SOC (see Supplementary Table VI), which we attribute to the effect of strong Te/I hybridization on the anisotropic exchange interactions that stabilize monolayer CrI_3's Ising-like ferromagnetism[50]. It is clear from the partial density of states in Fig. 3 that the (e_g) conduction bands of the bilayer with SOC have nearly equal Te and I p-orbital character, indicating strong hybridization. As the iodine SOC is instrumental in mediating the anisotropic exchange interactions which stabilize out-of-plane ferromagnetic order in monolayer CrI_3[50], this hybridization must enhance the exchange interactions in a way that ultimately increases the magnitude of the z-component of the magnetic moments on the Cr atoms. Strong interlayer e_g-e_g interactions in bilayer CrI_3 favor interlayer antiferromagnetic (AFM) coupling[51], so the observed AFM interlayer coupling along with strong hybridization between the Te and I p-orbitals with e_g character suggests a similar mechanism in this heterostructure.

Topological properties of ML 1T'-WTe_2 and BL WTe_2/CrI_3

To assess the potential for topology that can give rise to chiral edge states in our bilayer, we first examined the band structures of the individual monolayers and combined bilayer structure. Previous modeling has shown that 1T'-WTe_2 possesses a band crossing below the Fermi level, which gives rise to its nontrivial topology[43]. As a first step, we thus determined the band structures

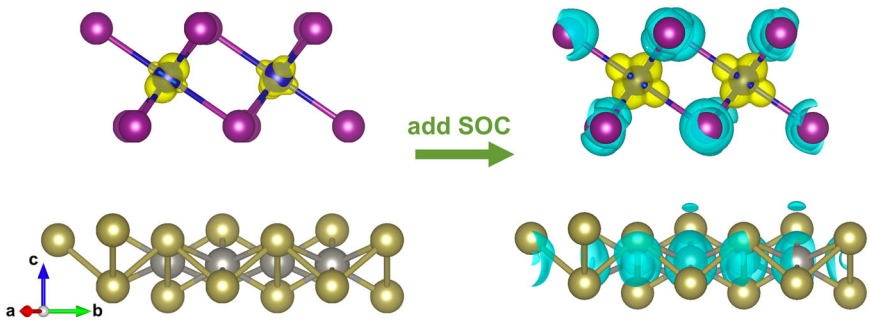

Fig. 4 Bilayer spin polarization is enhanced by spin-orbit coupling. Left: Collinear PBE+U spin density difference (yellow = positive) $s_{BL} - s_{CrI3} - s_{WTe2}$ with an isosurface level value of 0.0025 shows slightly enhanced positive magnetization on the Cr atoms due to spin-polarized charge transfer. **Right:** Noncollinear PBE+U magnetization density z-component difference (yellow = positive) $m_{BL} - m_{CrI3} - m_{WTe2}$ with an isosurface level value of 0.0025 shows more drastic Cr magnetization enhancement, and additionally magnetic induction in WTe_2.

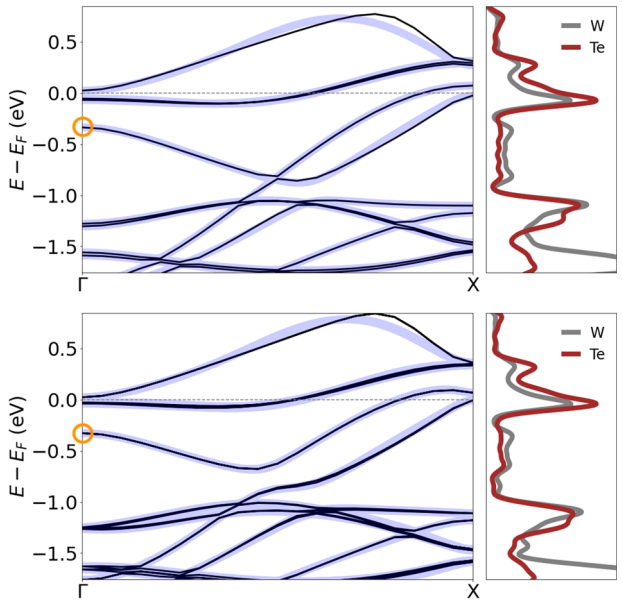

Fig. 5 Band structures of monolayer 1T'-WTe_2. Top: Collinear PBE band structure (black) and partial density of states (PDOS) of 0.8%-strained 1T'-WTe_2 (relative to bulk) with the interpolated MLWF band structure overlain in light blue. **Bottom:** Noncollinear PBE band structure with spin-orbit coupling.

of our strained WTe_2 monolayer with and without SOC to verify that our slight distortion does not change the bands significantly.

Indeed, as shown in Fig. 5, a band crossing occurs mid-way between the Γ and X high-symmetry points as is also observed in simulations of pristine WTe_2 without SOC. In addition, the density of states in this region has slightly more W d-orbital character than Te p-orbital character and is consistent with the previous assignment of these bands to the hybridized W $5d_{xz}$ and $5d_{z^2}$ orbitals[43]. These band structures confirm that the strain applied to the monolayer did not alter its topology. Integration of the Berry curvature over the fiber bundle of maximally localized Wannier functions (MLWFs) up to the band circled in Fig. 5 yields a Chern number of 0, meaning the topology is trivial as expected, since SOC was turned off. The same analysis of the noncollinear WTe_2 monolayer when SOC is included (bottom of Fig. 5) exhibits a band gap within the $5d_{xz}$ and $5d_{z^2}$ bands about halfway between the Γ and X high-symmetry points. Integration of the Berry curvature over the fiber bundle of these MLWFs yields a Chern number of 1, verifying that this monolayer is topologically nontrivial[43].

Next, we calculated the band structure, partial density of states, and Chern number for the bilayer composed of ML 1T'-WTe_2 and ML CrI_3 (Fig. 3) with and without SOC. This bilayer loses the Mott insulating behavior of CrI_3, with the bilayer exhibiting a metallic band structure and finite density of states at and around the Fermi level. The bilayer also maintains monolayer 1T'-WTe_2's band crossing below the Fermi level, which opens when SOC is introduced as is visible in the upper panel of Fig. 3. The integration of the Berry curvature over the fiber bundle of MLWF's up to and including the W $5d_{xz}$ and $5d_{z^2}$ orbitals yields a Chern number of 0, when spin-orbit coupling is not included in the DFT calculation, while the same process for the spin-orbit-coupled MLWFs also yields a Chern number of 0, indicating that this bilayer loses the topological character of monolayer 1T'-WTe_2 when CrI_3 is stacked on top of it.

Conductance in a model terraced 1T'-WTe_2/CrI_3 heterostructure

In principle, the bulk-boundary correspondence guarantees that a conducting edge must exist at the interface between topologically trivial and nontrivial regions of a system. In the spirit of completeness, we nevertheless performed a direct calculation of the conductance in a simplified model heterostructure, which suggests that even when interfacial scattering is considered, edge conductance persists at the boundary between monolayer WTe_2 and bilayer 1T'-WTe_2/CrI_3.

The schematic in Fig. 6 depicts the hopping sites in our model heterostructure, as well as the calculated current, which is overlain onto a transparent version of the same grid. The red portion of the grid is a semi-infinite lead representing the conducting bilayer, from and to which current flows. This portion is represented by a four-band model, which contains the four bands involved in the topological crossing of WTe_2[52] split by a magnetic field-induced potential that emulates the magnetic field produced by the proximate ferromagnetic monolayer CrI_3 (see Supplementary Information). The blue region is the scattering region of pristine monolayer 1T'-WTe_2, and it is represented by a four-band model which is the same as that of the lead except that it does not have the additional magnetic field-induced potential. Note that we do not include terms describing interlayer hybridization due to the fact that the primary effect of hybridization is to remove the topology of WTe_2, which was already established via our calculation of the Chern number in the bilayer portion of the terraced heterostructure. The length scale of our tight-binding model is set by the spacing of the grid points, which is equal to the lattice parameters of pristine ML 1T'-WTe_2 in units of Å.

Finally, we used the Kwant software package[53] to solve the scattering problem for the scattering matrix and eigenfunctions of our model heterostructure. We then constructed the current operator in terms of the scattering matrix at the energy at which

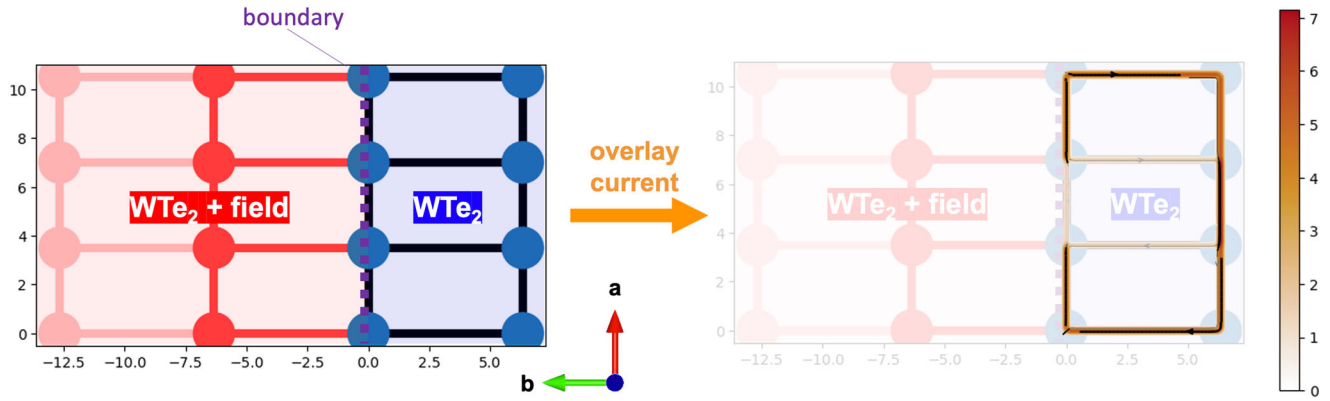

Fig. 6 Edge conductance persists on the exposed 1T′-WTe_2 monolayer of a model terraced heterostructure. Left: Top view of the sites in a simplified heterostructure in which the red region represents the lead corresponding to WTe_2 subject to the magnetic field produced by CrI_3 and the blue region is the scattering region of pristine ML WTe_2. **Right:** The calculated current (in varying shades of red) overlain on a transparent version of the model heterostructure is the largest around the edge of the pristine WTe_2.

the topological crossing occurs in the Kwant-computed band structure (see Supplementary Fig. 4), and calculated the conductance by applying this operator to the scattering eigenfunctions at that same energy and summing their contributions, obtaining a conductance of 7.0 e^2/h. When we plot the corresponding current in the right panel of Fig. 6, it is evident that the current mostly flows around the edge, consistent with previous conductance experiments on pristine monolayer 1 T'-WTe_2[43,54]. In addition, this current is down-spin (polarized) since the proximity of CrI_3 lowers the energy of the down-spin bands in ML WTe_2.

DISCUSSION

We have used a combination of density functional theory and MLWF-based tight-binding models to demonstrate that bilayer 1 T'-WTe_2/CrI_3 is a topologically nontrivial metallic material that exhibits enhanced Cr magnetic moments and spin-polarized charge transfer from WTe_2 to CrI_3. Most notably, the topologically nontrivial monolayer WTe_2 becomes trivial when a monolayer of CrI_3 is placed on top of it, and this is reflected in a Chern number of 1 for monolayer 1T'-WTe_2 and of 0 for the bilayer.

Since the constituent 1T'-WTe_2 layer is itself topological, this observation lends itself to the possibility of realizing a chiral edge state in a terraced 1T'-WTe_2/CrI_3 bilayer. According to the bulk-boundary correspondence[14,55], a chiral edge state should exist at the boundary between topologically trivial and topologically nontrivial materials. If we place half of a layer of CrI_3 atop a layer of WTe_2 to form a terraced bilayer, the Chern number should change from 0 in the bilayer to 1 as soon as the CrI_3 layer ends. This suggests that a chiral edge state should exist at this boundary. In addition, the magnetic field of the ferromagnetic CrI_3 should break the degeneracy of the two chiral edge states of the ML WTe_2, causing the step edge of CrI_3 to host a spin-polarized chiral edge state.

We further simulated the conduction of a simplified model of the terraced bilayer, finding that the edge conductance of WTe_2 is retained in such a heterostructure, and is spin polarized by the CrI_3. Taken together, our findings suggest that terraced bilayer 1 T'-WTe_2/CrI_3 in which a monolayer of 1T'-WTe_2 is partly covered by a monolayer of CrI_3 may exhibit a chiral conducting edge state and is thus a candidate for being a 2D topological spin filter. This is the first evidence for this type of behavior in a system composed of a nonmagnetic Weyl semimetal placed next to an atomically thin magnet, thus expanding the concept of such terraced chiral edge states beyond magnetic Weyl semimetal materials.

METHODS

In order to determine the ground electronic states of the constituent monolayers and 1T'-WTe_2/CrI_3 bilayer, as well as the charge transfer present in the bilayer, we calculated ground electronic states and charge and spin densities using self-consistent DFT. We then Wannierized the DFT orbitals we obtained into a form allowing for the calculation of Chern numbers, which determine whether a material is topologically nontrivial. Finally, we characterized the conduction observed in our heterostructure by extending a previously parameterized $\mathbf{k}\cdot\mathbf{p}$ model of 1T'-WTe_2 to a simplified version of our terraced heterostructure. As the different rhombohedral angles of monolayer $R3$ CrI_3 and 1T'-WTe_2 do not lend themselves to the simple construction of a commensurate supercell without the introduction of different strain to both layers, the layers were strained slightly by hand so that they could share a common cell. We therefore begin this methodology section by discussing the determination of the appropriate strain and interlayer distance of the bilayer before going into greater detail about the DFT calculations, the computation of the Chern numbers, and the details of our edge conductance simulations.

Bilayer supercell construction

To construct our bilayer, we used a highly accurate diffusion Monte Carlo (DMC)-optimized monolayer CrI_3 structure containing 8 atoms in its unit cell and exhibiting triclinic ($R3$) symmetry[56]. A monolayer 1T'-WTe_2 structure was obtained from the Materials Project website[57]. During the simulation of these monolayers, more than 20 Å of vacuum was added to both structures to prevent spurious self-interactions.

In stacking the layers, special consideration was given to how to align them since their monolayer structures are incommensurate. In particular, the WTe_2 cell was rotated such that the original lattice constants for the monolayer cells were strained as little as possible. The result of this process was a bilayer with a lattice constant of 7.01 Å, which means that our DMC-optimized ML CrI_3 structure is stretched by 2.5% relative to the monolayer, and WTe_2 ($a = 3.505$ Å) is stretched by 0.8% relative to the experimental bulk 1T'-WTe_2 value of 3.477 Å[58]. In addition, our monolayer 1T'-WTe_2 lattice constant is close to the value of 3.502 Å previously obtained using DFT structural relaxation[59].

Density functional simulations

All simulations of structural and electronic properties were performed using DFT as implemented within the Quantum ESPRESSO package[60,61]. The PBE and PBE+U functionals[62] with

$U = 2$ eV on the chromium atoms were selected to model these materials because previous studies demonstrated that a trial wavefunction utilizing a Hubbard U value of 2–3 eV minimizes the fixed-node error in DMC calculations of CrI_3[56,63]. Our calculations used norm-conserving, scalar-relativistic Cr and relativistic I pseudopotentials and recently developed spin-orbit relativistic effective W and Te pseudopotentials[64]. We employed a Monkhorst-Pack k-point mesh with dimensions $10 \times 10 \times 1$ and a plane wave energy cutoff of 300 Ry.

Calculating topological invariants

To calculate the Chern numbers for monolayer WTe_2 and the bilayer heterostructure, subsets of DFT single-particle Bloch functions were bijectively rotated onto sets of MLWFs[65] starting from selected columns of the density matrix from DFT via the SCDM-k method[66]. This mapping was performed for the isolated set of 31 monolayer $1T'$-WTe_2 bands ranging from −10 eV below to 0.6 eV above the monolayer Fermi level, and for entangled sets of bilayer $1T'$-WTe_2/CrI_3 bands as detailed in the Supplementary Information. All of the obtained MLWFs were well-localized and replicated the DFT band structure well over the span of bands involved in calculating topological invariants. Next, the hopping terms and correction terms for the lattice vectors of the hopping terms output by Wannier90 were used as input to the tight-binding model for the Z2Pack software for calculating topological invariants. Z2Pack is capable of calculating the evolution of hybrid Wannier charge centers across the surface defined by an explicit Hamiltonian $H(\mathbf{k})$, a tight-binding model, or an explicit first-principles calculation[67,68]. Thus, with our tight-binding model as input, we used Z2Pack to calculate the hybrid Wannier center evolution of the MLWF's corresponding to the bands up to and including the two orbitals involved in WTe_2's spin-orbit-induced gap opening[19] on a small k-space sphere with a radius of 0.001 centered at the Γ-point of the first Brillouin zone. All of the Z2Pack calculations passed the line and surface convergence checks to within the default tolerances of Z2Pack[67,68].

Simulating edge conductance

Lastly, in order to obtain more direct evidence that our heterostructure behaves like a topological spin filter, we modeled the edge conductance of ML $1T'$-WTe_2 by constructing a four-band $\mathbf{k} \cdot \mathbf{p}$ model, solving the corresponding scattering problem, and calculating the conductance of this model using the quantum transport software Kwant[53].

Our model consists of two regions: a semi-infinite conducting lead representative of BL $1T'$-WTe_2/CrI_3 and a scattering region representative of ML $1T'$-WTe_2, which are connected to one another. To mimic the magnetic field that would be induced by the CrI_3 in the bilayer portion, we subject half of the ML $1T'$-WTe_2 to a magnetic field. The bilayer portion of the Hamiltonian ignores hybridization between WTe_2 and CrI_3 (see the Results section for discussion). We provide the forms of the continuous Hamiltonians for the lead and scattering regions in the Supplementary Information.

Next, we discretized this model onto a rectangular grid with site spacing commensurate with ML WTe_2's lattice parameters: $a = 3.50$ Å and $b = 6.34$ Å. Both regions used previously reported $\mathbf{k} \cdot \mathbf{p}$ model parameters for pristine $1T'$-WTe_2[52], and the bilayer region contained an additional energy offset for the magnetic field-induced splitting of the WTe_2 bands. We then solved the scattering problem according to the Landauer-Büttiker formalism[53], and applied current operators to the resulting eigenfunctions to calculate the conductance.

DATA AVAILABILITY

The datasets used and/or analyzed during the current study are available from the corresponding author upon request.

Received: 11 August 2023; Accepted: 5 December 2023;
Published online: 15 April 2024

REFERENCES

1. Wolf, S. et al. Spintronics: a spin-based electronics vision for the future. *Science* **294**, 1488–1495 (2001).
2. Ahn, E. 2D materials for spintronic devices. *npj 2D Mater. Appl*. https://doi.org/10.1038/s41699-020-0152-0 (2020).
3. Zhang, S. et al. Two-dimensional heterostructures and their device applications: progress, challenges and opportunities. *J. Phys. D Appl. Phys.* **54**, 433001 (2021).
4. Zhang, T., Xu, X., Huang, B., Dai, Y. & Ma, Y. 2D spontaneous valley polarization from inversion symmetric single-layer lattices. *npj Comput. Mater*. https://doi.org/10.1038/s41524-022-00748-0 (2022).
5. El-Ghazalya, A., Gorchon, J., Wilson, R., Pattabi, A. & Bokor, J. Progress towards ultrafast spintronics applications. *J. Magn. Magn. Mater.* **502**, 166478 (2020).
6. Barla, P., Joshi, V. & Bhat, S. Spintronic devices: a promising alternative to CMOS devicess. *J. Comput. Electron.* **20**, 805–837 (2021).
7. Hirohataa, A. et al. Review on spintronics: principles and device applications. *J. Magn. Magn. Mater.* **509**, 166711 (2020).
8. Inomata, K. et al. Highly spin-polarized materials and devices for spintronics. *Sci. Technol. Adv. Mater.* **9**, 014101 (2008).
9. Béa, H., Gajek, M., Bibes, M. & Barthélémy, A. Spintronics with multiferroics. *J. Phys. Condens. Matter.* **20**, 434221 (2008).
10. Zhang, L., Wang, Y., Liu, X. & Liu, F. Electrical switching of spin-polarized current in multiferroic tunneling junctions. *npj Comput. Mater*. https://doi.org/10.1038/s41524-022-00886-5 (2022).
11. Massarotti, D. et al. Macroscopic quantum tunnelling in spin filter ferromagnetic Josephson junctions. *Nat. Commun*. https://doi.org/10.1038/s41524-022-00886-5 (2015).
12. Koga, T., Nitta, J. & Takayanagi, H. Spin-filter device based on the Rashba effect using a nonmagnetic resonant tunneling diode. *Phys. Rev. Lett.* **88**, 126601 (2002).
13. Cummings, A., Akis, R. & Ferry, D. Electron spin filter based on Rashba spin-orbit coupling. *Appl. Phys. Lett.* **89**, 172115 (2006).
14. Hasan, M. Z. & Kane, C. L. Colloquium: topological insulators. *Rev. Mod. Phys.* **82**, 3045 (2010).
15. Mak, K., Shan, J. & Ralph, D. Probing and controlling magnetic states in 2D layered magnetic materials. *Nat. Rev. Phys.* **1**, 646–661 (2019).
16. Yoshida, N. Theory of the spin-filtering effect in ferromagnet/ferromagnetic insulator/superconductor junctions. *J. Phys. Comm.* **3**, 045013 (2019).
17. Howard, S. et al. Evidence for one-dimensional chiral edge states in a magnetic weyl semimetal $Co_3Sn_2S_2$. *Nat. Commun*. https://doi.org/10.1038/s41467-021-24561-3 (2021).
18. Hsieh, T., Ishizuka, H., Balents, L. & Hughes, T. Bulk topological proximity effect. *Phys. Rev. Lett.* **116**, 086802 (2016).
19. Qian, X., Liu, J., Fu, L. & Li, J. Quantum spin hall effect in two-dimensional transition metal dichalcogenides. *Science* **346**, 1344–1347 (2014).
20. Sierra, J., Fabian, J., Kawakami, R., Roche, S. & Valenzuela, S. Van der Waals heterostructures for spintronics and opto-spintronics. *Nat. Nanotechnol.* **16**, 856–868 (2021).
21. Novoselov, K., Mishchenko, A., Carvalho, A. & Castro Neto, A. 2D materials and van der Waals heterostructures. *Science* https://doi.org/10.1126/science.aac9439 (2016).
22. Pham, P. et al. 2D heterostructures for ubiquitous electronics and optoelectronics: principles, opportunities, and challenges. *Chem. Rev.* **122**, 6514–6613 (2022).
23. He, F. et al. Moiré patterns in 2D materials: a review. *ACS Nano.* **15**, 5944–5958 (2021).
24. Xu, Y. et al. Coexisting ferromagnetic-antiferromagnetic state in twisted bilayer CrI_3. *Nat. Nanotechnol.* **17**, 143–147 (2022).
25. Morissette, E. et al. Dirac revivals drive a resonance response in twisted bilayer graphene. *Nat. Phys*. https://doi.org/10.1038/s41567-023-02060-0 (2023).
26. Fumega, A. & Lado, J. Moiré-driven multiferroic order in twisted $CrCl_3$, $CrBr_3$ and CrI_3 bilayers. *2D Mater.* **10**, 025026 (2023).
27. Dai, Z., Liu, L. & Zhang, Z. Strain engineering of 2D materials: Issues and opportunities at the interface. *Adv. Mater.* **31**, 1805417 (2019).
28. Maximenko, Y. et al. Nanoscale studies of electric field effects on monolayer 1T′-WTe_2. *npj Quantum Mater*. https://doi.org/10.1038/s41535-022-00433-x (2022).

29. Marmodoro, A. et al. Electric field control of magnons in magnetic thin films: ab initio predictions for two-dimensional metallic heterostructures. *Phys. Rev. B* **105**, 174411 (2022).
30. Tao, W. et al. Multiband superconductivity in strongly hybridized 1T -WTe_2/$NbSe_2$ heterostructures. *Phys. Rev. B* **105**, 094512 (2022).
31. Iordanidou, K. et al. Electric field and strain tuning of 2D semiconductor van der Waals heterostructures for tunnel field-effect transistors. *ACS Appl. Mater. Interfaces* **15**, 1762–1771 (2023).
32. Karpan, V. et al. Graphite and graphene as perfect spin filters. *Phys. Rev. Lett.* **99**, 176602 (2007).
33. Piquemal-Banci, M. et al. 2D-MTJs: introducing 2D materials in magnetic tunnel junctions. *J. Phys. D. Appl. Phys.* **50**, 203002 (2017).
34. Cobas, E. et al. Graphene as a tunnel barrier: graphene-based magnetic tunnel junctions. *Nano Lett.* **12**, 3000–3004 (2012).
35. Song, T. et al. Giant tunneling magnetoresistance in spin-filter van der Waals heterostructures. *Science* **360**, 1214–1218 (2018).
36. Wang, Z. et al. Very large tunneling magnetoresistance in layered magnetic semiconductor CrI_3. *Nat. Commun.* https://doi.org/10.1038/s41467-018-04953-8 (2018).
37. Klein, D. et al. Probing magnetism in 2D van der Waals crystalline insulators via electron tunneling. *Science* **360**, 1218–1222 (2018).
38. Zhu, Y. et al. Giant tunneling magnetoresistance in van der Waals magnetic tunnel junctions formed by interlayer antiferromagnetic bilayer $CoBr_2$. *Phys. Rev. B* **103**, 134437 (2021).
39. Luo, B. et al. Stacking order, perfect spin polarization, and giant magnetoresistance in zigzag graphene/h-BN heterobilayer nanoribbons. *Phys. Rev. Appl.* **19**, 034002 (2023).
40. Li, Q. et al. Stacking- and strain-dependent magnetism in Janus CrSTe bilayer. *Appl. Phys. Lett.* **122**, 121902 (2023).
41. Li, Y. et al. Nonvolatile electrical control of spin polarization in the 2D bipolar magnetic semiconductor VSeF. *npj Comput. Mater.* https://doi.org/10.1038/s41524-023-01005-8 (2023).
42. Feng, J. et al. Excellent spin-filtering and giant tunneling magnetoresistance in a dual-electrode van der Waals magnetic tunnel junction based on ferromagnetic $CrSe_2$. *Appl. Surf. Sci.* **611**, 155588 (2023).
43. Tang, S. et al. Quantum spin Hall state in monolayer 1T′-WTe_2. *Nat. Phys.* **13**, 683–687 (2017).
44. MacNeill, D. et al. Control of spin-orbit torques through crystal symmetry in WTe_2/ferromagnet bilayers. *Nat. Phys.* **13**, 300–305 (2017).
45. Li, P. et al. Spin-momentum locking and spin-orbit torques in magnetic nano-heterojunctions composed of Weyl semimetal WTe_2. *Nat. Commun.* https://doi.org/10.1038/s41467-018-06518-1 (2018).
46. Chang, C. Marriage of topology and magnetism. *Nat. Mater.* **19**, 484–485 (2020).
47. Zhao, W. et al. Magnetic proximity and nonreciprocal current switching in a monolayer WTe2 helical edge. *Nat. Mater.* **19**, 503–507 (2020).
48. Bora, M., Mohanty, S., Singh, A., Gao, W. & Deb, P. Adaptive half-metallicity via magnetic proximity in an electrically sensitive 1T′-WTe_2/$CrBr_3$ vdW heterostructure. *Appl. Surf. Sci.* **623**, 157019 (2023).
49. Huang, B. et al. Layer-dependent ferromagnetism in a van der Waals crystal down to the monolayer limit. *Nature* **546**, 270–273 (2017).
50. Lado, J. & Fernández-Rossier, J. On the origin of magnetic anisotropy in two dimensional CrI_3. *2D Mater.* **4**, 035002 (2017).
51. Jang, S., Jeong, M., Yoon, H., Ryee, S. & Han, M. Microscopic understanding of magnetic interactions in bilayer CrI_3. *Phys. Rev. Mater.* **3**, 031001 (2019).
52. Shi, L. & Song, J. Symmetry, spin-texture, and tunable quantum geometry in a WTe_2 monolayer. *Phys. Rev. B* **99**, 035403 (2019).
53. Groth, C., Wimmer, M., Akhmerov, A. & Waintal, X. Kwant: a software package for quantum transport. *New J. Phys.* **16**, 063065 (2014).
54. Fei, Z. et al. Edge conduction in monolayer WTe_2. *Nat. Phys.* **13**, 677–682 (2017).
55. Essin, A. & Gurarie, V. Bulk-boundary correspondence of topological insulators from their respective Green's functions. *Phys. Rev. B* **84**, 125132 (2011).
56. Staros, D. et al. A combined first principles study of the structural, magnetic, and phonon properties of monolayer CrI_3. *J. Chem. Phys.* **156**, 014707 (2022).
57. Jain, A. et al. Commentary: The materials project: a materials genome approach to accelerating materials innovation. *APL Mater.* **1**, 011002 (2013).
58. Mar, A., Jobic, S. & Ibers, J. Metal-metal vs tellurium-tellurium bonding in WTe_2 and its ternary variants $TaIrTe_4$ and $NbIrTe_4$. *J. Am. Chem. Soc.* **114**, 8963–8971 (1992).
59. Xiang, H. et al. Quantum spin Hall insulator phase in monolayer WTe_2 by uniaxial strain. *AIP Advances* **6**, 095005 (2016).
60. Giannozzi, P. et al. QUANTUM ESPRESSO: a modular and open-source software project for quantum simulations of materials. *J. Phys. Condens. Matter* **21**, 395502 (2009).
61. Giannozzi, P. et al. Advanced capabilities for materials modelling with quantum ESPRESSO. *J. Phys. Condens. Matter* **29**, 465901 (2017).
62. Perdew, J. P., Burke, K. & Ernzerhof, M. Generalized gradient approximation made simple. *Phys. Rev. Lett.* **77**, 3865–3868 (1996).
63. Ichibha, T., Dzubak, A., Krogel, J., Cooper, V. & Reboredo, F. CrI_3 revisited with a many-body ab initio theoretical approach. *Phys. Rev. Mater.* **5**, 064006 (2021).
64. Guangming, W. et al. A new generation of effective core potentials from correlated and spin-orbit calculations: Selected heavy elements. *J. Chem. Phys.* **157**, 054101 (2022).
65. Marzari, N. & Vanderbilt, D. Maximally localized generalized Wannier functions for composite energy bands. *Phys. Rev. B* **56**, 12847 (1997).
66. Damle, A., Lin, L. & Ying, L. SCDM-k: Localized orbitals for solids via selected columns of the density matrix. *J. Comput. Phys.* **334**, 1–15 (2017).
67. Soluyanov, A. & Vanderbilt, D. Computing topological invariants without inversion symmetry. *Phys. Rev. B* **83**, 235401 (2011).
68. Gresch, D. et al. Z2pack: Numerical implementation of hybrid wannier centers for identifying topological materials. *Phys. Rev. B* **95**, 075146 (2017).

ACKNOWLEDGEMENTS

D.S. was funded by the U.S. Department of Energy through the Office of Science Graduate Student Research (SCGSR) Program. The funder played no role in study design, data collection, analysis and interpretation of data, or the writing of this manuscript. B.R.'s effort was supported by the U.S. Department of Energy, Office of Science, Basic Energy Sciences, Materials Sciences and Engineering Division, as part of the Computational Materials Sciences Program and Center for Predictive Simulation of Functional Materials. P.G. was supported by the U.S. Department of Energy, Office of Basic Energy Sciences, Scientific User Facilities Division as part of the QIS Infrastructure Project "Precision Atomic Assembly for Quantum Information Science". Research on model building and DFT calculations was performed at the Center for Nanophase Materials Sciences (CNMS), which is a US Department of Energy, Office of Science User Facility at Oak Ridge National Laboratory. This project used resources of the Oak Ridge Leadership Computing Facility under Contract No. DE-AC05-00OR22725 and of the National Energy Research Scientific Computing Center under Contract No. DE-AC0205CH11231, both U.S. Department of Energy Office of Science User Facilities.

AUTHOR CONTRIBUTIONS

P.G. initiated and co-supervised the research. Simulations and analysis were performed by D.S.; the manuscript was prepared by D.S. and B.R. All authors read, edited, and approved the final manuscript.

COMPETING INTERESTS

The authors declare no competing interests.

ADDITIONAL INFORMATION

Supplementary information The online version contains supplementary material available at https://doi.org/10.1038/s44306-023-00007-y.

Correspondence and requests for materials should be addressed to Daniel Staros, Brenda Rubenstein or Panchapakesan Ganesh.

Reprints and permission information is available at http://www.nature.com/reprints

Publisher's note Springer Nature remains neutral with regard to jurisdictional claims in published maps and institutional affiliations.